Energy-momentum transfer in the free-electron–photon interaction mediated by a film

Wentao Wang,[1,2] Dingguo Zheng,[1] Siyuan Huang,[1,2] Jun Li,[1] Yongzhao Zhang,[1,2] Taimin Miao,[1,2] Shuaishuai Sun,[1] Huanfang Tian,[1] Huaixin Yang,[1,2] and Jianqi Li[1,2,3,*]

[1]*Beijing National Laboratory for Condensed Matter Physics, Institute of Physics, Chinese Academy of Sciences, Beijing 100190, China*
[2]*School of Physical Sciences, University of Chinese Academy of Sciences, Beijing 100049, China*
[3]*Songshan Lake Materials Laboratory, Dongguan, Guangdong 523808, China*

(Received 7 September 2023; revised 25 December 2023; accepted 11 March 2024; published 8 April 2024)

The ultrafast transmission electron microscope equipped with an electron energy spectrometer provides a platform to study the electron-photon interaction in both the energy and momentum dimensions. Here, we analyzed the fraction of inelastically scattered electrons and the energy-momentum exchange in the free-electron–photon interaction mediated by a Ag/Si_3N_4 bilayer thin film. Taking advantage of the high transverse coherence electrons emitted by the laser-driven Schottky field emission gun, the quantized transverse momentum transfer was characterized in reciprocal space. We report experimental data on the relatively large transverse momentum transfer caused by momentum spread in free-electron–photon interactions. The momentum uncertainty of the photons guarantees momentum matching and provides an effective way to control the magnitude of the transverse momentum quanta by tilting the film, demonstrating the potential for controlling the free-electron wave function in momentum space.

DOI: 10.1103/PhysRevB.109.134305

I. INTRODUCTION

Since the development of photon-induced near-field electron microscopy (PINEM) [1], the coherent free-electron–photon interaction has attracted much attention for manipulating the free-electron wave function. Information about the electromagnetic field distribution is imprinted on the electron wave function, providing an approach to manipulate electrons with pulsed or continuous lasers [2,3]. After the interaction, the longitudinal phase of the electron is sinusoidally modulated, resulting in modulation of the energy spectrum [4,5]. Energy selection of the electrons is used to image the near-field distribution [6–8], image the probe cavity modes [9,10], and characterize the surface plasmon polaritons (SPPs) [11–17] or phonon polaritons [18]. Attosecond pulse trains [19,20] and coherent quantum-state control [21] in longitudinal phase space have also been studied.

Regarding the transverse direction, several results have been reported in recent years. The transverse momentum transfer in the electron-photon (e-p) interaction [22,23] and generation of electron vortex beams carried with orbital angular momentum by chiral SPPs have been investigated [24,25]. In addition, shaping the electron beam by shaped optical fields [26] and externally controlled SPPs [27,28] has been reported in theory and by experiment. Previous studies have demonstrated the ability of optical fields to shape electron wave packets, motivating further investigation of the momentum transfer process in the free-e–p interaction.

In this study, the e-p interaction mediated by a Ag/Si_3N_4 bilayer thin film was investigated with the field-emission ultrafast transmission electron microscope (UTEM). The energy states of the free electrons inelastically scattered by photons were analyzed by electron energy-loss spectroscopy (EELS). The energy-momentum matching guaranteed by the uncertainty principle was revealed in the free-e–p interaction, and the experimental setup-dependent transverse momentum exchange demonstrated the control of the free-electron quantum wave function in reciprocal space.

II. ENERGY TRANSFER IN THE FREE-ELECTRON–PHOTON INTERACTION

The layout of the experiments is shown in Fig. 1. In the UTEM, free-electron pulses were emitted by the laser-driven Schottky field emission gun, and the angle between the photoelectron beam and the pump laser beam was 90 °. The electron pulses were collimated and traversed the laser-illuminated sample, and the energy and transverse momentum changes after interaction were characterized by EELS and in reciprocal space, respectively [Fig. 1(a)]. The sample in the experiments was a 18-nm-thick Ag film on a 10-nm-thick Si_3N_4 film (see Appendix A), which was supported by a silicon transmission electron microscopy (TEM) window and mounted on a double-tilt holder to realize rotation around the y axis (tilt angle θ) and x' axis (tilt angle α) [Fig. 1(b)].

Over the last decade, the e-p coherent interaction has been extensively studied. As pulsed electrons pass through the confined electromagnetic field, the electromagnetic field modulates the phase of the electron wave function and induces Rabi oscillations of the electron populations in multilevel quantum energy states [29]. This can be characterized by EELS, which shows a series of discrete peaks. These peaks are on either side of the zero-loss peak (ZLP), and they are separated by one photon energy.

*Corresponding author: ljq@aphy.iphy.ac.cn

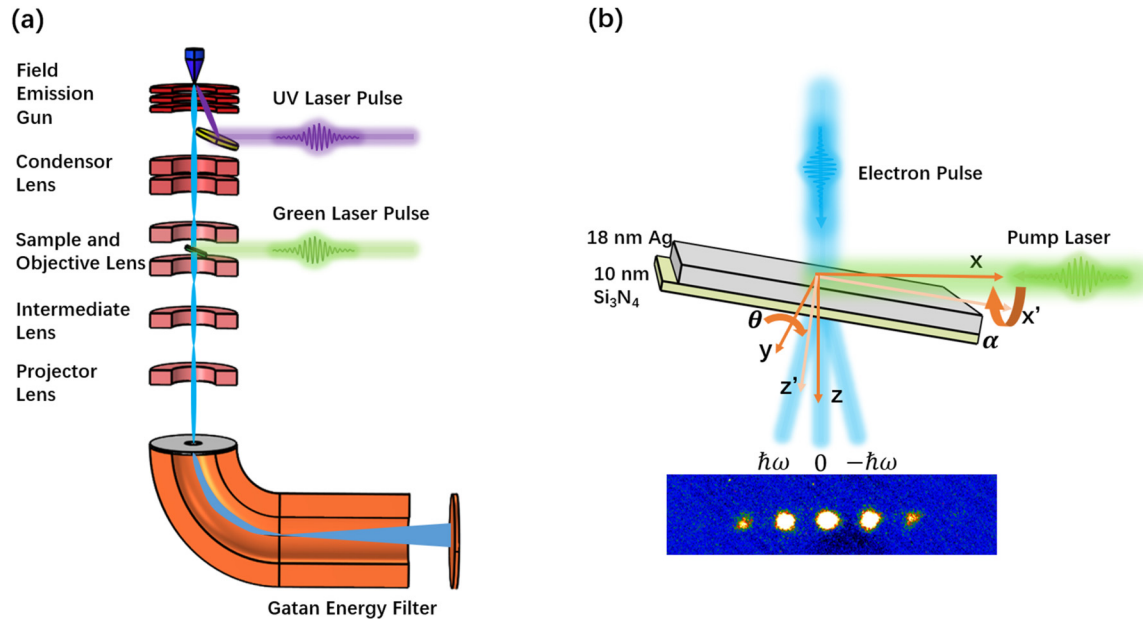

FIG. 1. Schematic of the layout of the experiments. (a) Schematic diagram of the UTEM apparatus. The photoelectron is emitted by a field-emission gun driven by a 260-nm laser beam. The wavelength of the pump laser is 520 nm (approximately 2.4 eV per photon). The direction of the pump laser is perpendicular to the electron beam. The UTEM operates in diffraction mode. (b) Coordinate setup. We denote (x, y, z) as the fixed laboratory coordinates and (x', y', z') as the rotated sample coordinates. The electron beam is incident along the z axis, and the pump laser is incident in the direction of $-x$. The transverse momentum distribution is analyzed in reciprocal space.

The normalized EELS data showing the e-p interactions caused by the Ag/Si_3N_4 bilayer plane with different angles θ at $\alpha = 0^\circ$ are shown in Fig. 2(a). To characterize the e-p interactions over a large θ range, a custom-built sample holder (see Fig. 6) was used in the experiment. After the interaction, the sidebands from the absorption (or emission) of up to four photons can be clearly identified when θ is greater than 25°, while the sidebands from the absorption (or emission) of only one photon can be observed when θ is less than 5°. The fraction of electrons that absorbed or emitted photons relative to the number of incident electrons is shown in Fig. 2(b), which was extracted from Fig. 2(a). Figure 2(b) gives the quantitative result of the dependence of the e-p coupling strength on θ, showing a steep increase at small tilt angle θ, which is mainly attributed to the change of the reflection phase (see Appendix B).

Nanomaterial-mediated free-e–p interactions have been well studied [4,6]. According to PINEM theory, the e-p coupling strength can be quantified by the factor β:

$$\beta(x, y) = \frac{e}{2\hbar\omega} \int_{-\infty}^{+\infty} E_z(x, y, z) e^{-i(\omega/v_e)z} dz, \qquad (1)$$

where E_z is the electric field component along the propagating direction of the electron pulses, ω is the circular frequency of the pump laser, $\hbar$ is the reduced Planck constant, and v_e is the relativistic velocity of the electron. The probability of an electron absorbing or emitting n photons is given by $P_n = J_n^2(2|\beta|)$, where J_n are nth-order Bessel functions of the first kind. The e-p coupling strength depends on E_z, and it can be changed by tilting the sample. Since the duration of the electron pulses in our experiment was longer than the duration of the laser pulses, the spatial and temporal distributions of the electrons and photons should be taken into account. For the simulation, we applied extended PINEM theory [30] to include the Gaussian distribution of the pump laser and free-electron pulses, and we calculated the probabilities and corresponding EELS spectra of the free electrons inelastically scattered by the pump laser (see Appendix B). The simulated results [Figs. 2(c) and 2(d)] were in good agreement with the experimental results [Figs. 2(a) and 2(b)].

Similar to previous work [22,23,31–33], the energy transfer observed here is the direct inelastic scattering of the electrons by the light waves. Physically, energy exchange between a free electron and the electromagnetic wave only occurs when the wave vector is matched. Wave vector matching can be satisfied by introducing a structure that supports the localized surface plasmon, surface plasmon polariton, phonon polariton, and cavity modes, thereby inhibiting the phase velocity of the photons. Another approach is to tailor the electromagnetic wave by periodic nanostructures to precisely satisfy the energy-momentum conservation requirement, such as the case in dielectric laser accelerators [34]. Here, the Ag/Si_3N_4 bilayer thin film is transparent to electrons but opaque to incident photons, providing a discontinuous electric field along the trajectory of the free electrons and increasing the momentum uncertainty of the photons to allow the e-p interaction to occur.

III. TRANSVERSE MOMENTUM TRANSFER IN THE FREE-ELECTRON–PHOTON INTERACTION

The energy transfer in the e-p interaction should be accompanied by momentum transfer. In PINEM theory, the final electron wave function after interaction with monochromatic light has the factor $e^{i[(p_0+n\hbar\omega/v_e)z-(E_0+n\hbar\omega)t]/\hbar}$, where p_0 and E_0 are the initial momentum and energy, respectively [6].

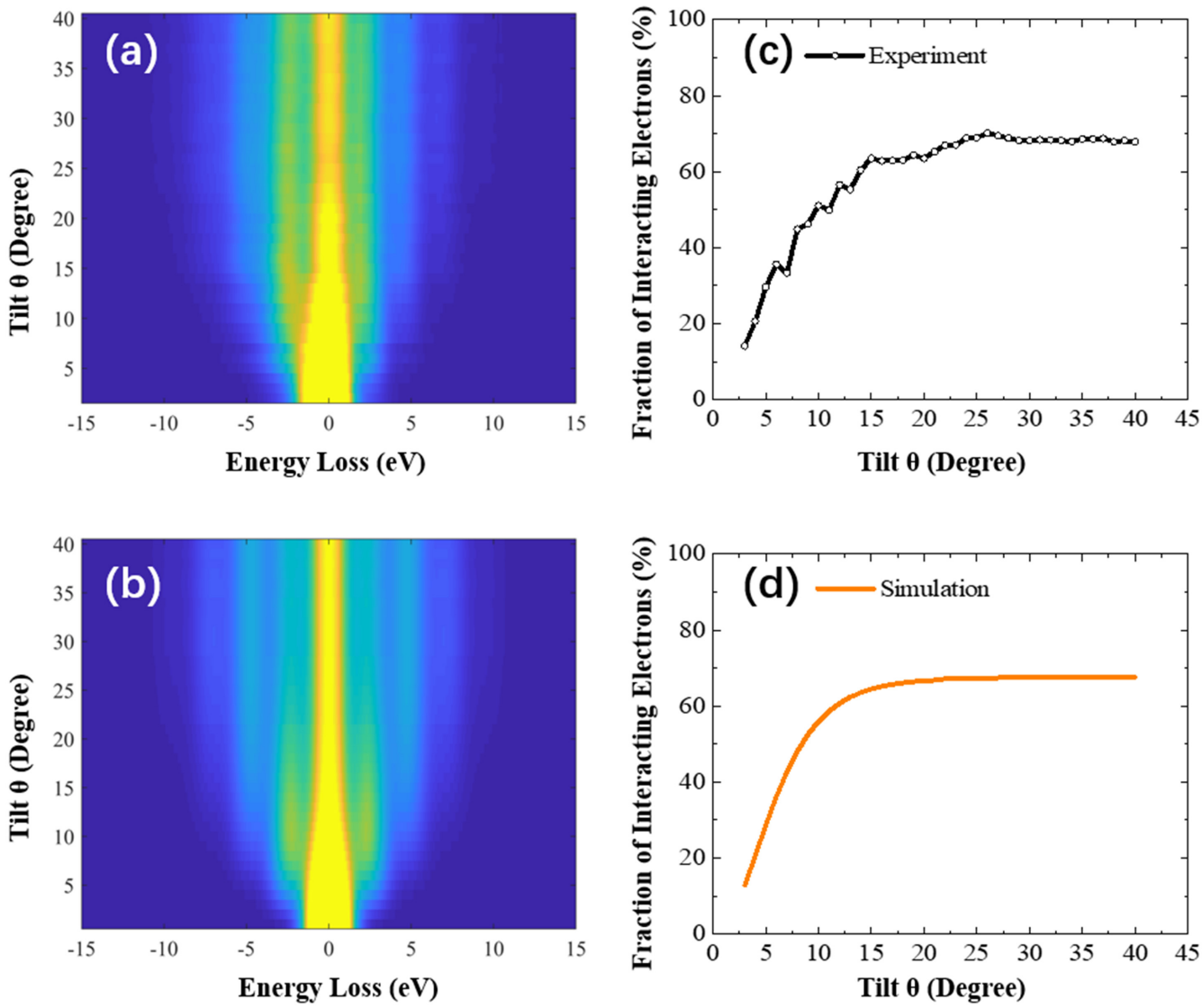

FIG. 2. Probabilities and corresponding EELS spectra obtained from the experiments and simulations. A *p*-polarized pump laser (electric field parallel to the z axis) with a peak field amplitude of 2.28×10^8 V/m was used in the experiments. (a) Experimental and (b) simulated normalized EELS spectra with $\theta = 3^\circ$ to 40° and $\alpha = 0^\circ$ plotted as color maps. (c) Experimental and (d) simulated results of the fraction of electrons that absorb or emit photons relative to the number of incident electrons as a function of θ. The simulation was performed with a peak field amplitude of 1.97×10^8 V/m to obtain the best agreement between simulation and experiment.

The exponential term indicates the exchange in the energy and longitudinal momentum quanta given by $n\hbar\omega$ and $\frac{n\hbar\omega}{v_e}$. However, transverse momentum is not taken into account in conventional PINEM theory, because the transverse momentum change of the subrelativistic electron is negligible.

Observing the transverse momentum of the electron after the e-p interaction is challenging. Owing to the small momentum of the photon compared with that of the subrelativistic electron, the deflection angle of electrons is typically a few microradians. Such a small angle requires high angle resolution for experimental characterization. In the experiment, high transverse coherence photoelectrons are emitted by the laser-driven Schottky field emission gun [35], which guarantees high angle resolution. Furthermore, the laser direction is perpendicular to the electron direction [see the top panel in Fig. 1(b)] to achieve the maximum transverse momentum exchange.

The high-dispersion diffraction (HDD) mode in the UTEM was used at a camera length of 80 m to obtain the far-field electron distribution in reciprocal space. When electron pulses and laser pulses simultaneously arrived on the bilayer film, certain electrons were deflected by photons and a series of equally spaced and collinear electron spots were well resolved in the momentum space [see the bottom panel of Fig. 1(b)]. The map of the energy loss and transverse momentum showed that there was a one-to-one correspondence between the quantized energy and the discrete transverse momentum of the scattered electrons (see Fig. 9).

Importantly, the transverse momentum transfer in the e-p coherent interaction is not constant, but it depends on the uncertainty principle and the energy-momentum conservation law. The far-field electron distributions in reciprocal space for different tilt angles are shown in Fig. 3. The distance between two electron spots increased with increasing θ in the direction

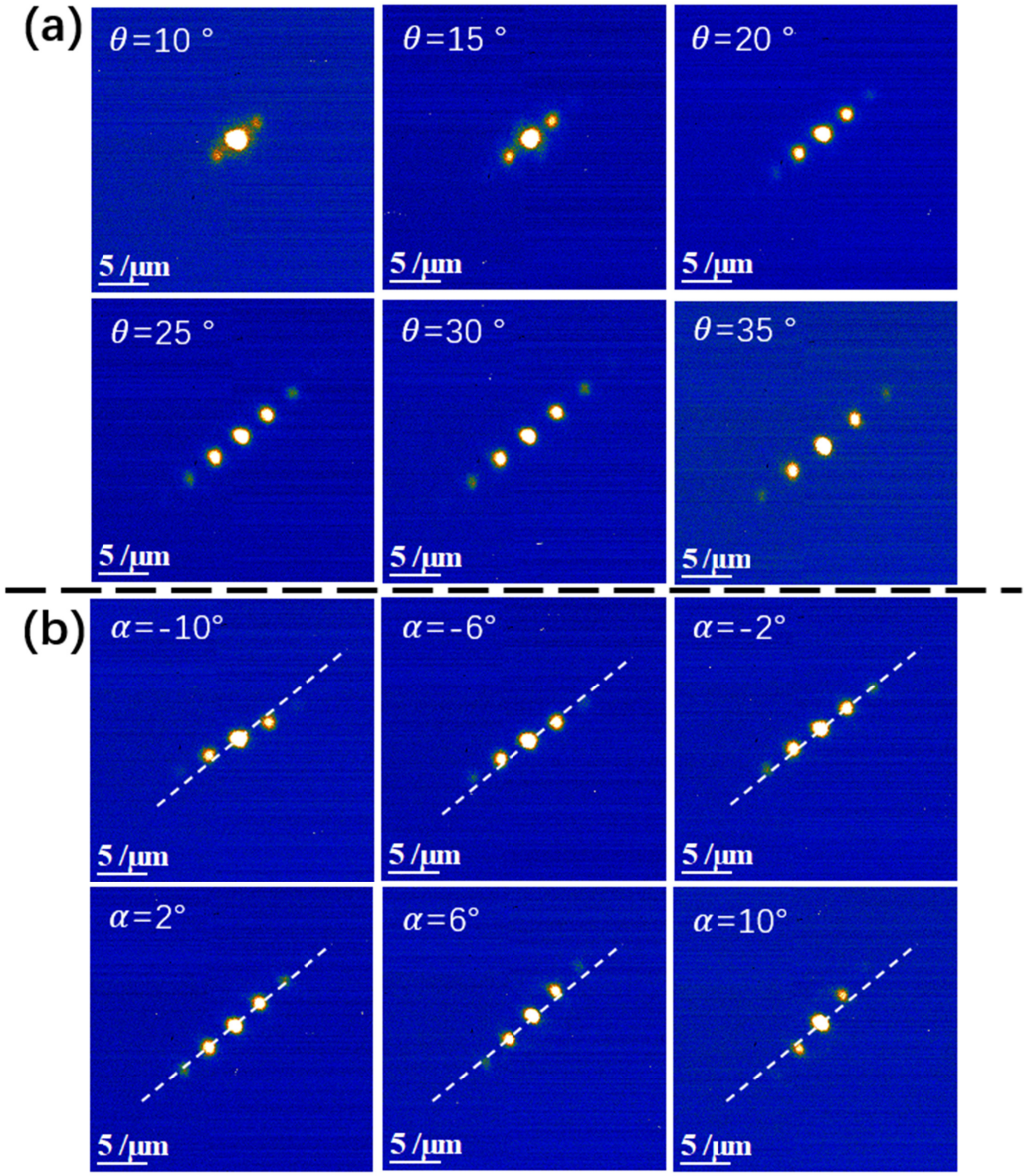

FIG. 3. Far-field electron distributions in reciprocal space after the e-p interaction when the film was at (a) $\alpha = 0^\circ$ with $\theta = 10^\circ$ to 35° and (b) $\theta = 25^\circ$ with $\alpha = -10^\circ$ to 10°. The white dashed lines in (b) indicate the direction of the laser, which serves as a reference to indicate the direction of the transverse momentum. The scale bars in all of figures were calibrated with a grating replica of 463 nm.

of the laser beam [Fig. 3(a)], indicating that the transverse momentum of the electrons increased with increasing θ after the electrons interacted with the photons. The distance between two electron spots changed little with α, while the direction of the transverse momentum significantly changed [Fig. 3(b)].

Further insight can be obtained with an analytical theory (see Appendix D). In the geometry of the experiments, the initial photons only had transverse momentum because the laser direction was perpendicular to the electron direction. The translation invariance in the direction parallel to the sample guarantees the determined transverse momentum, which appears as discrete electron spots in reciprocal space. However, the direction perpendicular to the sample is limited, which results in momentum spreading [36]. The photon momentum spreading provides the longitudinal momentum quanta $\frac{\hbar\omega}{v_e}$, and hence energy-momentum matching. According to theoretical analysis, the dependence of the transverse momentum on θ and α is given by

$$p_x^{'} = -\hbar k_0 \left(1 + \frac{c}{v_e}\tan\theta\right), \tag{2}$$

$$p_y^{'} = \hbar k_0 \frac{c}{v_e}\frac{\tan\alpha}{\cos\theta}, \tag{3}$$

where p_x' and p_y' are the transverse momentum along the x axis and y axis, respectively. k_0 is the wave vector of the pump laser in vacuum. The distance between two electron spots in reciprocal space is $k_\perp = \frac{1}{\hbar}\sqrt{p_x^{'2} + p_y^{'2}}$, and the angle between the direction of the transverse momentum and the direction of the laser (direction deviation) is $\gamma = \arctan(\frac{p_y'}{p_x'})$. We obtained the experimental and theoretical results for the magnitude and direction deviation of the transverse momentum

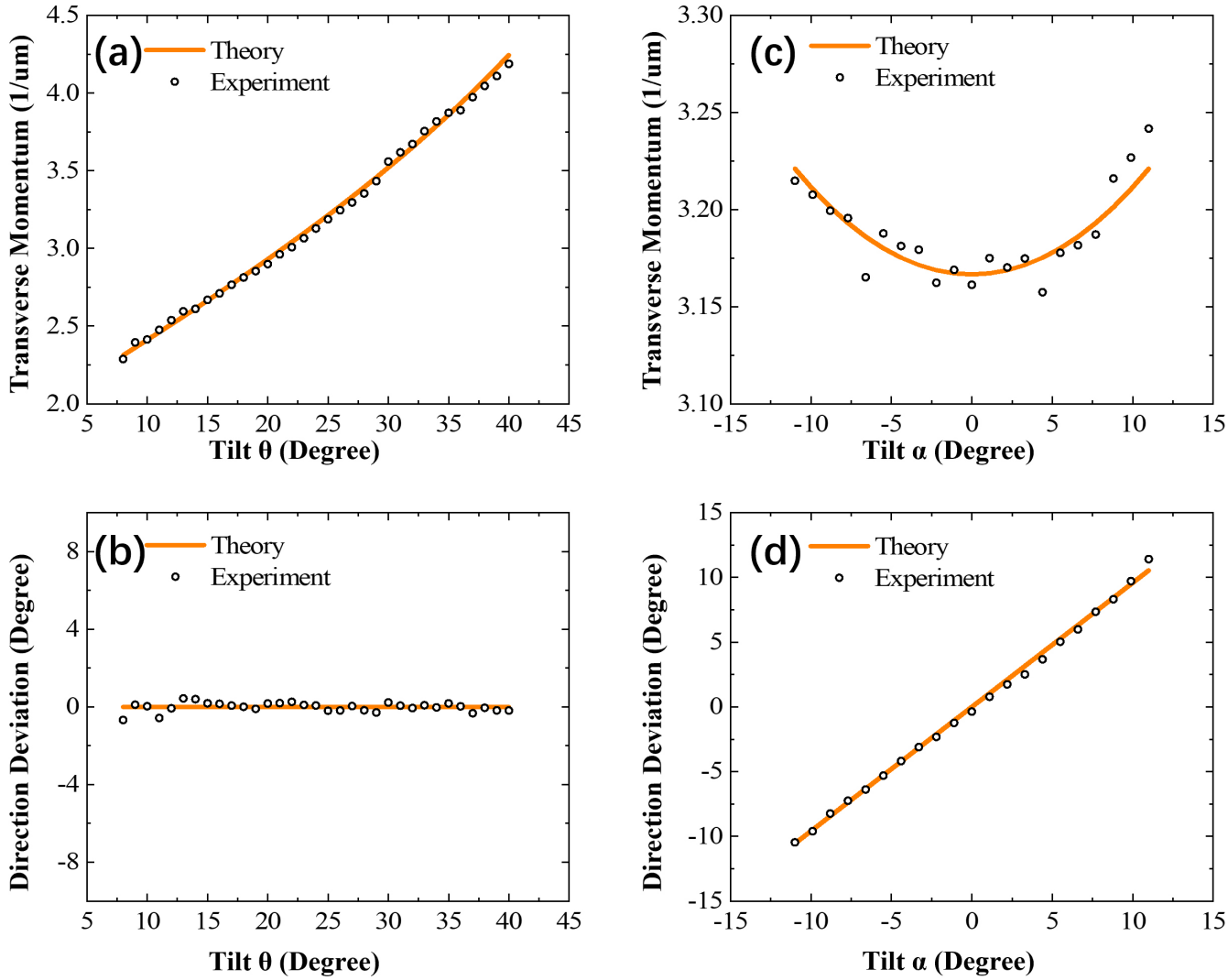

FIG. 4. Theoretical and experimental results for different tilt angles. (a) Magnitude and (b) direction deviation of the transverse momentum for $\alpha = 0^\circ$ with $\theta = 8^\circ$ to 40°. (c) Magnitude and (d) direction deviation of the transverse momentum for $\theta = 25^\circ$ with $\alpha = -11^\circ$ to 11°. The orange lines are the theoretical results and the black circles are the experimental results.

when the film was at $\alpha = 0^\circ$ with $\theta = 8^\circ$ to 40° and $\theta = 25^\circ$ with $\alpha = -11^\circ$ to 11°. The theoretical results were in good agreement with the experimental results (Fig. 4).

IV. DISCUSSION AND CONCLUSION

We have demonstrated that the film-mediated e-p inelastic scattering process depends on the quantum nature of the electron and is governed by the quantum mechanical uncertainty principle, rather than the classical process in which electrons are deflected by the electromagnetic field. The multiphoton emission or absorption process is guaranteed by the energy-momentum conservation, which is satisfied over a wide range of electron energies and exhibits a series of discrete transverse momentums in reciprocal space. The magnitude of the transverse momentum quanta depends on the momentum spread of the photons. In Eq. (2), the first term $\hbar k_0$ is the initial momentum of the photons, and the second term $\frac{\hbar\omega}{v_e}\tan\theta$ originates from the uncertainty of the photon momentum in the perpendicular film direction. Similarly, p_y' in Eq. (3) is the component of the momentum spread on the y axis.

Film-mediated free-electron momentum modulation by an optical field can be expressed as

$$\boldsymbol{p} = (0,\ 0,\ p_0) \rightarrow \boldsymbol{p} = \left(np_x',\ np_y',\ p_0 + \frac{n\hbar\omega}{v_e}\right). \tag{4}$$

This transform indicates that three-dimensional phase modulation of the free electron wave function can be achieved with extreme precision. The experiment demonstrated that the geometry of the laser direction perpendicular to the electron direction in the UTEM has a unique advantage in observing the transverse momentum exchange of the e-p interaction. By tilting the sample around the y axis, the transverse momentum increased, resulting in improved observability in reciprocal space. For $v_e \approx 0.695c$, the transverse momentum increases by approximately 2.2 times as θ changes from 2° to 40°. Importantly, the transverse coherence of the electrons emitted by the laser-driven Schottky field emission gun is only slightly affected by the space charge effect, which allows high angular

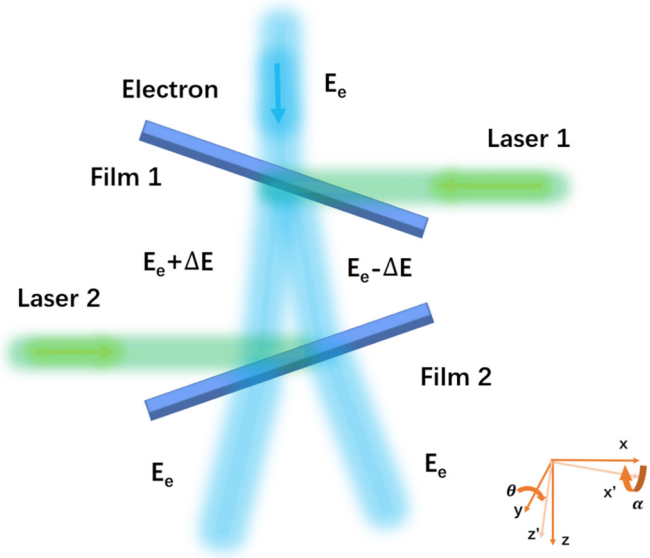

FIG. 5. Layout of the tunable coherent beam splitter. The coordinate setup is illustrated in the bottom right corner, which is the same as in Fig. 1(b). The electron beam is incident along the z axis. Laser 1 is incident along the $-x$ direction, while laser 2 is incident in the x direction.

resolution to be maintained while using a high electron dose. The high angle resolution of the UTEM, enhanced by the experimental geometry, provides a different dimension for characterizing the e-p interaction than EELS. It shows the ability to characterize low-energy photons, which is limited by the energy resolution, and to identify time zero in the UTEM without an electron energy spectrometer.

Such tunable transverse momentum provides a simple way to control the angle and direction of inelastic electron-light scattering, and it shows the ability to act as a tunable electron splitter over a wide range. Based on the experimental results obtained in our measurements, we can conceptually propose a tunable coherent beam splitter that can deflect electrons without changing their energy, which will be verified in our future experiments. A conceptual design of the experiments is shown in Fig. 5. An electron beam (blue) passes through the two spatially separated films, which are illuminated in the opposite direction by two coherent laser beams (green). The tilt angles of the film 1 and film 2 can be set to (θ, α) and $(-\theta, -\alpha)$, respectively. The free electrons interact sequentially with the two phase-locked laser beams. Each of the two interactions imposes a sinusoidal phase modulation on the electron wave function, yielding an integrated effect of the two modulations. The enhancement or cancellation of the coupling depends on the relative phase of the two laser beams. In order to obtain the output electron beams with the same energy, we can set the phase difference of two laser beams to be π to ensure that the total coupling constant is equal to 0. For the transverse momentum transfer, we consider two electrons that absorb and emit a photon (Fig. 5), respectively. At the film 2, since the total coupling constant is equal to 0, the electron that absorbed/emitted a photon in the first interaction will emit/absorb a photon in the second interaction. It is noted that the transverse momentum acquired in the two interactions occurs in the opposite direction, thus the electrons can be deflected after two interactions.

In conclusion, we have systematically studied the free-e–p coherent interaction mediated by a Ag/Si_3N_4 bilayer film. Electrons can interact with photons owing to the momentum spread caused by the discontinuity of the electric field at the sample. The fractions of interacting electrons with different field intensities and different tilt angles were obtained by EELS. Extended PINEM theory was used to calculate the fractions of inelastically scattered electrons and was in good agreement with the experimental results. By using the HDD mode in the UTEM, we directly accessed the transverse momentum space and found a one-to-one correspondence between the quantized energy and the transverse momentum transfer in the interaction process. We reported the relationship between longitudinal and transverse momentum in the free-electron–photon interaction; in particular, the energy-momentum conservation was carefully analyzed in correlation with the transverse momentum spread. This feature could also be important for achieving precise three-dimensional modulation of free electrons. Tilting the film provides an effective way to tune the magnitude and direction of the electron transverse momentum. These results demonstrate the potential in controlling the transverse momentum of electrons.

ACKNOWLEDGMENTS

This project was supported by the National Natural Science Foundation of China (Grants No. U22A6005, No. 12074408, No. 52271195, and No. 11921004), the National Key Research and Development Program of China (Grant No. 2021YFA1301502), the Strategic Priority Research Program (B) of the Chinese Academy of Sciences (Grants No. XDB25000000 and No. XDB33000000), the Scientific Instrument Developing Project of the Chinese Academy of Sciences (Grants No. YJKYYQ20200055, No. ZDKYYQ2017002, and No. 22017BA10), the Synergetic Extreme Condition User Facility (SECUF), Beijing Municipal Science and Technology major project (Grant No. Z201100001820006), and Institute of Physics, Chinese Academy of Sciences Hundred Talents Program (Grant No. Y9K5051).

APPENDIX A: EXPERIMENTAL SETUP

The experiments were performed with the ultrafast transmission electron microscope (UTEM) based on a commercial JEOL-2100F Schottky field-emission microscope equipped with a Gatan Quantum 965 imaging filter. The 1040-nm 300-fs initial laser pulses were propagated through two β-barium borate crystals and split into two laser beams by a dichroic mirror. A frequency-doubled laser (520 nm) was used to excite the sample, and a frequency-quadrupled laser (260 nm) was introduced into the field emission gun to generate the photoemission. The free-electron pulses were accelerated to 200 keV and propagated along the z axis, while the direction of the pump laser was along the $-x$ direction. More details have been reported elsewhere [35]. The energy distribution was recorded by a postcolumn spectrometer with a typical exposure time of 100 s. The high dispersion diffraction (HDD)

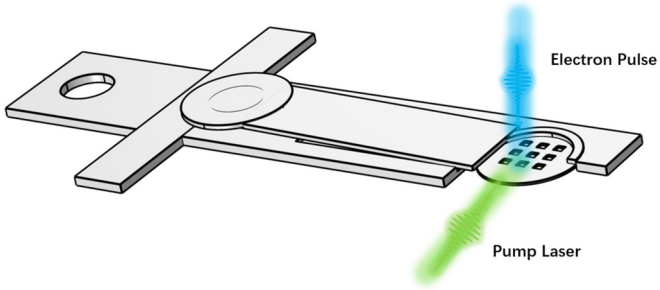

FIG. 6. Schematic of the custom-built transmission electron microscope holder. The laser-facing side of the sample holder tip was removed, allowing the laser to be incident at the lowest θ of 3°.

was recorded by a charge-coupled device (CCD) after the electron energy spectrometer with a typical exposure time of 100 s.

The Ag/Si_3N_4 bilayer film was fabricated by thermally depositing an 18-nm-thick Ag thin film on a 10-nm-thick Si_3N_4 membrane supported by a Si TEM window with an 80 μm × 80 μm aperture. A custom-built TEM sample holder was used to extend the range of the angle θ (Fig. 6).

APPENDIX B: PROBABILITY OF ELECTRON INELASTIC SCATTERING BY THE PUMP LASER

To simulate the EELS spectra obtained in the experiment, the spatial and temporal distributions of the pump laser and free electrons should be considered. Since conventional PINEM theory only considers the spatial dependence of the electron and laser, we applied extended PINEM theory [30] to the calculation to include the spatiotemporal dependence. According to extended PINEM theory, the generalized time-dependent coupling constant is

$$\beta(x,y,t)=\frac{e}{\hbar\omega}\int_{-\infty}^{+\infty}\tilde{E}_z\left(x,y,z;t+\frac{z}{v_e}\right)e^{-i(\omega/v_e)z}dz, \quad \text{(B1)}$$

where t is the time in the frame of reference associated with the electron. The electric field component along the propagation direction of the electron pulses can be expressed as $E_z(\boldsymbol{r},t)=\tilde{E}_z(\boldsymbol{r},t)e^{-i\omega t}$, where $\tilde{E}_z$ is the complex electric field phasor, and the physical field is $2\mathrm{Re}\{\tilde{E}_z(\boldsymbol{r},t)\}$. The coherent electron probability density is given by

$$\rho^{\mathrm{coherent}}(x,y,U,\Delta t)=\sum_n P_n^{\mathrm{coherent}}(x,y,\Delta t)\delta(U-n\hbar\omega), \quad \text{(B2)}$$

where $P_n^{\mathrm{coherent}}(x,y,\Delta t)=J_n^2(2|\beta(x,y,\Delta t)|)$ is the probability of an electron absorbing or emitting n photons and Δt is the time delay between the electron and laser.

In our experiment, we used a near-parallel traveling electron beam, and the radius of the electron beam was approximately 0.5 μm. While the full width at half maximum (FWHM) values of the Gaussian pump laser in the transverse and propagation directions were approximately 80 and 90 μm (corresponding to 300 fs), respectively, the spatial distribution of the incident electron pulses was negligible. We then set the Gaussian center in the transverse direction and the propagation direction of the laser at the origin when $t=0$ [see Fig. 1(b)] and performed the calculation in the $x-z$ plane to simulate the experimental data in Figs. 2(a) and 2(b).

Considering the Ag/Si_3N_4 bilayer thin film used in the experiment, the distribution of the electromagnetic field can be divided into four parts. The z component of the incident electric field is

$$E_i^z(x,y,z,t)=E_0e^{-z^2/2\sigma_l}e^{-[-x/c-t]^2/2\sigma_t}e^{-ik_0x-i\omega t}, \quad \text{(B3)}$$

where E_0 is the peak field intensity of the incident laser, σ_t is the duration of the laser pulse, and σ_l is the standard deviation of the laser's spatial Gaussian distribution. The z component of the reflective electric field is

$$\begin{aligned}E_r^z(x,y,z,t)=&rE_0\cos(2\theta)e^{-[-x\sin(2\theta)+z\cos(2\theta)]^2/2\sigma_l}\\&\times e^{-\{-x/c-[x\cos(2\theta)+z\sin(2\theta)]/c-t\}^2/2\sigma_t}\\&\times e^{-ik_0[x\cos(2\theta)+z\sin(2\theta)]-i\omega t},\end{aligned} \quad \text{(B4)}$$

where $r=|r|e^{i\delta_{r,TM}}$ is the transverse magnetic reflection coefficient of the bilayer film. Because the bilayer film is thin, the spatial and temporal deviation of the laser's Gaussian center caused by the film can be ignored. The z component of the transmitted electric field is

$$E_t^z(x,y,z,t)=t'E_0e^{-z^2/2\sigma_l}e^{-(-x/c-t)^2/2\sigma_t}e^{-ik_0x-i\omega t}, \quad \text{(B5)}$$

where $t'=|t'|e^{i\delta_{t'}}$ concludes the intensity and phase change of the electric field at the exit point of the electron beam relative to the incident point. r,t', and the z component of the electric field in the film $E_f^z(x,y,z,t)$ can be calculated by the transfer matrix method (TMM) [37]. Then the integral in $\beta(x=0,y=0,t)$ can be calculated by Eq. (B1).

We note that the physical origin of the steep increase in the fraction of interacting electrons [see Fig. 2(c)] at small tilt angle θ is mainly due to the reflection phase $\delta_{r,TM}$. Without loss of generality, we used the time-averaged electric field $\bar{E}_0$ to include the distribution of the pump laser in the propagation direction. For small tilt angles, $|r|\approx 1$, $|t'|\approx 0$, and $\cos(2\theta)\approx 1$. Thus, we can ignore the electric field in the film and rewrite Eq. (B1) as

$$\begin{aligned}\beta(x=0,y=0)=&\frac{e}{\hbar\omega}\int_{-\infty}^{0}\bar{E}_0e^{-z^2/2\sigma_l}\\&\times(1+e^{i\delta_{r,TM}}e^{-ik_0z\sin(2\theta)})e^{-i(\omega/v_e)z}dz.\end{aligned} \quad \text{(B6)}$$

Since the factor $k_0\sin(2\theta)\ll\omega/v_e$, it can be ignored. We then obtain $|\beta(\theta)|\propto|1+e^{i\delta_{r,TM}}|$. Since $\delta_{r,TM}\approx 173°$ at $\theta=1°$ and $\delta_{r,TM}$ decreases as θ increases, $|\beta(\theta)|$ increases with increasing θ [Fig. 7(b)].

To simulate the experimental data, the initial distribution of the incident electron pulse in terms of time and energy should be included. Since the energy bandwidth of a single electron wave packet is narrow compared with the incoherent energy bandwidth, the time and energy terms can be decomposed, and the time distribution is a standard Gaussian:

$$g(u,t)=\frac{1}{\sigma_e\sqrt{2\pi}}e^{-(1/2)(t/\sigma_e)^2}A(u), \quad \text{(B7)}$$

where σ_e is the duration of the electron pulse and $A(u)$ is the zero-loss peak (ZLP) in EELS. The final electron probability density function is obtained by convolving the coherent single

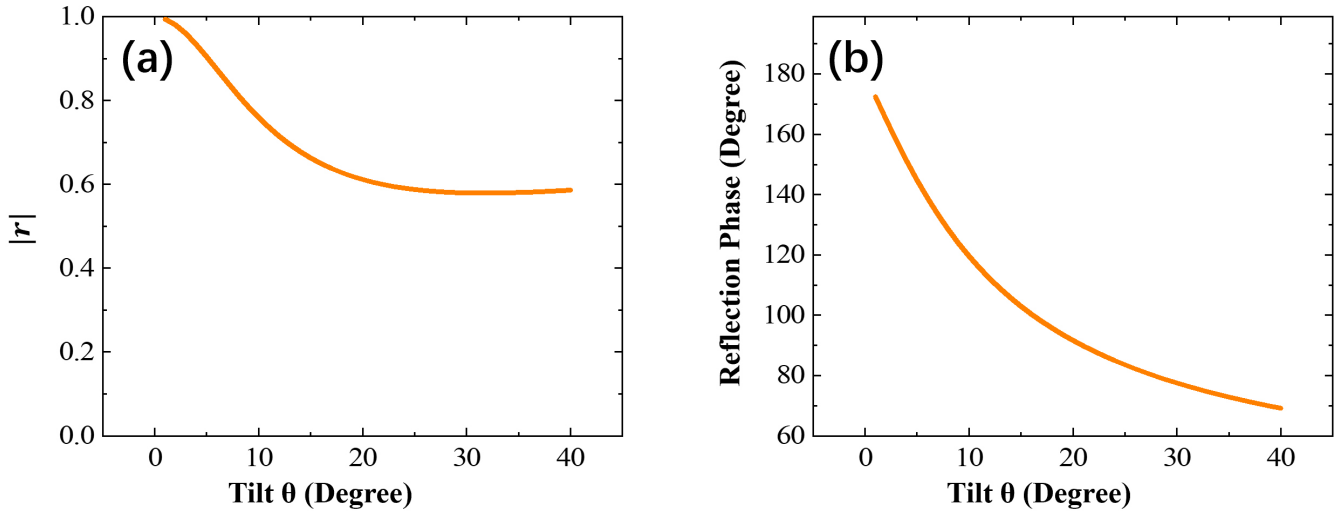

FIG. 7. The transverse magnetic reflection coefficient of the bilayer film. (a) Magnitude of the reflection coefficient $|r|$ and (b) reflection phase $\delta_{r,TM}$ as a function of the tilt angle θ.

electron probability density and incoherent initial electron probability density in time and energy:

$$\rho(x, y, u, \Delta t) = \iint g(U, T) \times \rho^{\text{coherent}}(x, y, u - U, \Delta t - T) dU dT. \quad \text{(B8)}$$

For the simulation, we used the relative permittivities of Ag and Si_3N_4 of $-8.91 + 0.28i$ [38] and 4.24 [39], respectively. The FWHM values of the Gaussian laser pulse in the transverse and propagation directions were 80 μm and 300 fs, respectively. The FWHM of the Gaussian electron pulse in the propagation direction was approximately 450 fs. The FWHM of the ZLP in EELS was 2.1 eV. The simulation results with $\Delta t = 0$ and a peak field amplitude of 1.97×10^8 V/m, which is approximately 90% of the experimental peak field for the best agreement between simulation and experiment, are shown in Fig. 2. The experimental results with a peak amplitude of 1.8×10^8 V/m are shown in Figs. 8(a) and 8(c), while the simulation results with a peak amplitude of 1.56×10^8 V/m are shown in Figs. 8(b) and 8(d).

APPENDIX C: ONE-TO-ONE CORRESPONDENCE BETWEEN THE QUANTIZED ENERGY AND DISCRETE TRANSVERSE MOMENTUM

To characterize the electron beam after the electron-photon (e-p) coherent interaction in both the energy and momentum dimensions, we rotated the diffraction pattern to be parallel to the EELS slit by tuning the projector lens current. A typical far-field electron distribution in reciprocal space after rotation is shown in Fig. 9(a). The FWHM of the transmitted electron beam was approximately 1.04 μm^{-1}, which was calibrated with a grating replica of 463 nm. Since the distance between two electron spots was approximately 3.88 μm^{-1}, all of the spots were separated and well resolved. The map of the energy loss and transverse momentum is shown in Fig. 9(b), where the electron spots stretched along the energy axis owing to the limited energy resolution of the electron spectrometer and the energy distribution of the initial electron beam. Figure 9(a), which was obtained by a CCD in HDD mode, and Fig. 9(c), which was obtained by an electron energy spectrometer, characterize the electrons after the e-p interaction in the momentum and energy dimensions, respectively, while Fig. 9(b) correlates the energy and transverse momentum of each spot in the energy-momentum space, showing a one-to-one correspondence between the quantized energy and discrete transverse momentum.

APPENDIX D: ANALYTICAL THEORY OF THE ENERGY-MOMENTUM TRANSFER IN THE FREE-ELECTRON–PHOTON INTERACTION MEDIATED BY THE FILM

In this section, we present an analytical explanation of the transverse momentum change of the electrons in Fig. 3 by considering the momentum uncertainty perpendicular to the sample and the energy-momentum conservation of the e-p interaction. We denote (x, y, z) as the fixed laboratory coordinates and (x', y', z') as the rotated sample coordinates [see Fig. 1(b)]. In the experiment, we first rotated the sample about the y axis, and we then rotated it about the x' axis. We consider the situation where a free electron absorbs a photon without loss of generality. The rotation matrix for transforming the fixed laboratory coordinates to the rotated sample coordinates is

$$\hat{R} = \begin{pmatrix} \cos\theta & 0 & \sin\theta \\ \sin\theta\sin\alpha & \cos\alpha & -\cos\theta\sin\alpha \\ -\sin\theta\cos\alpha & \sin\alpha & \cos\theta\cos\alpha \end{pmatrix}. \quad \text{(D1)}$$

The momentum of the incident light in the sample coordinate is

$$\boldsymbol{p}_{(x',y',z')} = \hat{R}\boldsymbol{p}_{(x,y,z)} = \hbar k_0 \begin{pmatrix} -\cos\theta \\ -\sin\theta\sin\alpha \\ \sin\theta\cos\alpha \end{pmatrix}, \quad \text{(D2)}$$

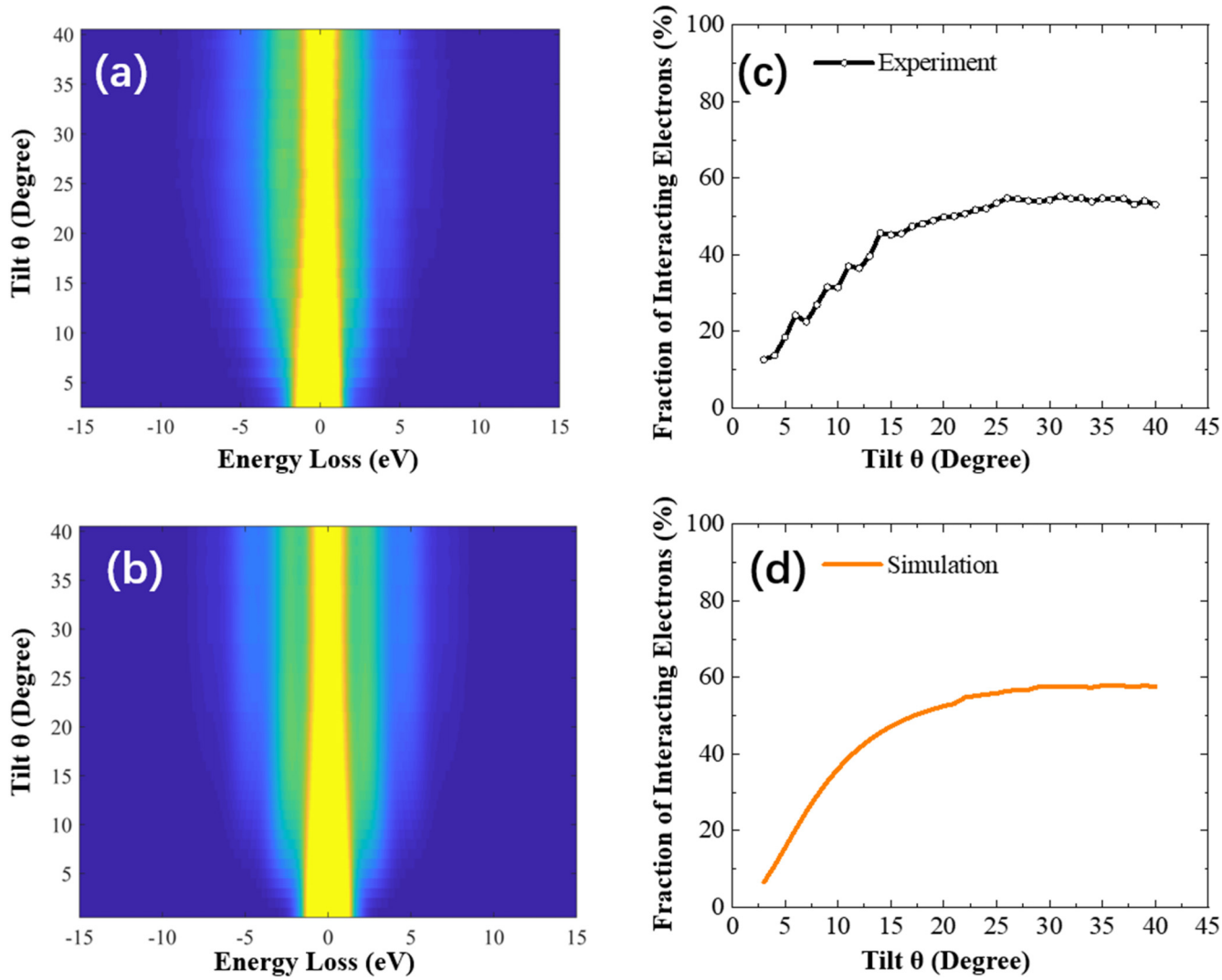

FIG. 8. Probabilities and corresponding EELS spectra obtained from the experiments with a peak amplitude of 1.8×10^8 V/m and simulations with a peak amplitude of 1.56×10^8 V/m. (a) Experimental and (b) simulated EELS spectra, and the corresponding (c) experimental and (d) simulated probability of electron inelastic scattering by the pump laser.

where $\boldsymbol{p}_{(x,y,z)} = \hbar k_0 \begin{pmatrix} -1 \\ 0 \\ 0 \end{pmatrix}$ is the momentum of the incident light in the laboratory coordinates (x, y, z) and $k_0 = \frac{\omega}{c}$ is the wave vector of the incident light. In view of the translational invariance in the direction parallel to the sample and the confined space in the direction perpendicular to the sample, the photon momentum spreads along z'. We then rewrite $\boldsymbol{p}_{(x',y',z')}$ as

$$\boldsymbol{p}'_{(x',y',z')} = \hbar \begin{pmatrix} -k_0 \cos\theta \\ -k_0 \sin\theta \sin\alpha \\ k' \end{pmatrix}, \tag{D3}$$

where k' is unknown. In laboratory coordinates,

$$\begin{aligned} \boldsymbol{p}'_{(x,y,z)} &= \hat{R}^{-1} \boldsymbol{p}'_{(x',y',z')} \\ &= \hbar \begin{pmatrix} -k_0 \cos^2\theta - k_0 \sin^2\theta \sin^2\alpha - k' \sin\theta \cos\alpha \\ -k_0 \sin\theta \sin\alpha \cos\alpha + k' \sin\alpha \\ -k_0 \sin\theta \cos\theta \cos^2\alpha + k' \cos\theta \cos\alpha \end{pmatrix}. \end{aligned} \tag{D4}$$

Taking energy-momentum conservation into account, only the photons with longitudinal momentum $\hbar\omega/v_e$ can be absorbed by electrons. We then solve k' as

$$k' = \frac{k_0}{\cos\theta \cos\alpha} \left(\frac{c}{v_e} + \sin\theta \cos\theta \cos^2\alpha \right). \tag{D5}$$

Finally, we obtain the expressions of the transverse momentum p'_x and p'_y by substituting Eq. (D5) into Eq. (D4), given by

$$p'_x = -\hbar k_0 \left(1 + \frac{c}{v_e} \tan\theta \right), \tag{D6}$$

$$p'_y = \hbar k_0 \frac{c}{v_e} \frac{\tan\alpha}{\cos\theta}, \tag{D7}$$

respectively.

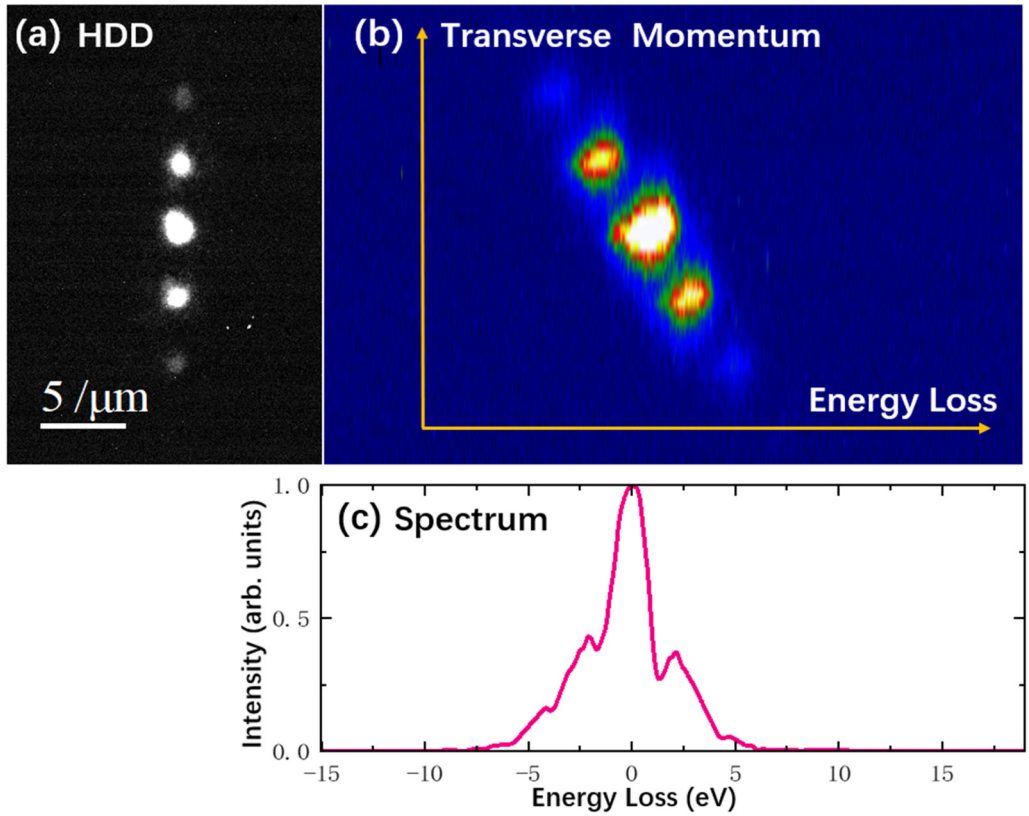

FIG. 9. Energy-momentum correlation map when the film was at $\theta = 35^\circ$ and $\alpha = 0^\circ$ for a *p*-polarization pump laser. (a) Far-field electron distribution in reciprocal space after tuning the projector lens current. (b) Map of the energy loss and transverse momentum taken by the CCD camera after the electron energy spectrometer in EELS mode. The vertical axis is the momentum axis, and the horizontal axis is the energy axis. (c) EELS spectrum taken by the electron energy spectrometer. The scale bar in (a) was calibrated with a grating replica of 463 nm.

[1] B. Barwick, D. J. Flannigan, and A. H. Zewail, Photon-induced near-field electron microscopy, Nature (London) **462**, 902 (2009)

[2] R. Dahan, A. Gorlach, U. Haeusler, A. Karnieli, O. Eyal, P. Yousefi, M. Segev, A. Arie, G. Eisenstein, P. Hommelhoff, and I. Kaminer, Imprinting the quantum statistics of photons on free electrons, Science **373**, eabj7128 (2021).

[3] J.-W. Henke, A. S. Raja, A. Feist, G. Huang, G. Arend, Y. Yang, F. J. Kappert, R. N. Wang, M. Möller, J. Pan, J. Liu, O. Kfir, C. Ropers, and T. J. Kippenberg, Integrated photonics enables continuous-beam electron phase modulation, Nature (London) **600**, 653 (2021).

[4] F. J. García de Abajo, A. Asenjo-Garcia, and M. Kociak, Multiphoton absorption and emission by interaction of swift electrons with evanescent light fields, Nano Lett. **10**, 1859 (2010).

[5] O. Reinhardt and I. Kaminer, Theory of shaping electron wavepackets with light, ACS Photonics **7**, 2859 (2020).

[6] S. T. Park, M. Lin, and A. H. Zewail, Photon-induced near-field electron microscopy (PINEM): Theoretical and experimental, New. J. Phys. **12**, 123028 (2010).

[7] A. Yurtsever, J. S. Baskin, and A. H. Zewail, Entangled nanoparticles: Discovery by visualization in 4D electron microscopy, Nano Lett. **12**, 5027 (2012).

[8] A. Yurtsever, R. M. van der Veen, and A. H. Zewail, Subparticle ultrafast spectrum imaging in 4D electron microscopy, Science **335**, 59 (2012).

[9] K. Wang, R. Dahan, M. Shentcis, Y. Kauffmann, A. Ben Hayun, O. Reinhardt, S. Tsesses, and I. Kaminer, Coherent interaction between free electrons and a photonic cavity, Nature (London) **582**, 50 (2020).

[10] O. Kfir, H. Lourenço-Martins, G. Storeck, M. Sivis, T. R. Harvey, T. J. Kippenberg, A. Feist, and C. Ropers, Controlling free electrons with optical whispering-gallery modes, Nature (London) **582**, 46 (2020).

[11] L. Piazza, T. T. A. Lummen, E. Quiñonez, Y. Murooka, B. W. Reed, B. Barwick, and F. Carbone, Simultaneous observation of the quantization and the interference pattern of a plasmonic near-field, Nat. Commun. **6**, 6407 (2015).

[12] T. T. A. Lummen, R. J. Lamb, G. Berruto, T. LaGrange, L. Dal Negro, F. J. García de Abajo, D. McGrouther, B. Barwick, and F. Carbone, Imaging and controlling plasmonic interference fields at buried interfaces, Nat. Commun. **7**, 13156 (2016).

[13] X. Fu, Z. Sun, S. Ji, F. Liu, M. Feng, B.-K. Yoo, and Y. Zhu, Nanoscale-femtosecond imaging of evanescent surface plasmons on silver film by photon-induced near-field electron microscopy, Nano Lett. **22**, 2009 (2022).

[14] I. Madan, G. M. Vanacore, E. Pomarico, G. Berruto, R. J. Lamb, D. McGrouther, T. T. A. Lummen, T. Latychevskaia, F. J. García de Abajo, and F. Carbone, Holographic imaging of electromagnetic fields via electron-light quantum interference, Sci. Adv. **5**, eaav8358 (2019).

[15] D. Zheng, S. Huang, C. Zhu, P. Xu, Z. Li, H. Wang, J. Li, H. Tian, H. Yang, and J. Li, Nanoscale visualization of a photoinduced plasmonic near-field in a single nanowire by free electrons, Nano Lett. **21**, 10238 (2021).

[16] S. Huang, P. Xu, D. Zheng, J. Li, H. Tian, H. Yang, and J. Li, Plasmonic near-field spatiotemporal characterizations of an asymmetric copper bowtie nanostructure, Appl. Phys. Lett. **122**, 111102 (2023).

[17] E. Pomarico, I. Madan, G. Berruto, G. M. Vanacore, K. P. Wang, I. Kaminer, F. J. G. de Abajo, and F. Carbone, meV resolution in laser-assisted energy-filtered transmission electron microscopy, ACS Photonics **5**, 759 (2018).

[18] Y. Kurman, R. Dahan, H. H. Sheinfux, K. Wang, M. Yannai, Y. Adiv, O. Reinhardt, L. H. G. Tizei, S. Y. Woo, J. Li, J. H. Edgar, M. Kociak, F. H. L. Koppens, and I. Kaminer, Spatiotemporal imaging of 2D polariton wave packet dynamics using free electrons, Science **372**, 1181 (2021).

[19] K. E. Priebe, C. Rathje, S. V. Yalunin, T. Hohage, A. Feist, S. Schäfer, and C. Ropers, Attosecond electron pulse trains and quantum state reconstruction in ultrafast transmission electron microscopy, Nat. Photon. **11**, 793 (2017).

[20] Y. Morimoto and P. Baum, Diffraction and microscopy with attosecond electron pulse trains, Nat. Phys. **14**, 252 (2018).

[21] K. E. Echternkamp, A. Feist, S. Schäfer, and C. Ropers, Ramsey-type phase control of free-electron beams, Nat. Phys. **12**, 1000 (2016).

[22] G. M. Vanacore, I. Madan, G. Berruto, K. Wang, E. Pomarico, R. J. Lamb, D. McGrouther, I. Kaminer, B. Barwick, F. J. García de Abajo, and F. Carbone, Attosecond coherent control of free-electron wave functions using semi-infinite light fields, Nat. Commun. **9**, 2694 (2018).

[23] A. Feist, S. V. Yalunin, S. Schäfer, and C. Ropers, High-purity free-electron momentum states prepared by three-dimensional optical phase modulation, Phys. Rev. Res. **2**, 043227 (2020).

[24] G. M. Vanacore, G. Berruto, I. Madan, E. Pomarico, P. Biagioni, R. J. Lamb, D. McGrouther, O. Reinhardt, I. Kaminer, B. Barwick, H. Larocque, V. Grillo, E. Karimi, F. J. García de Abajo, and F. Carbone, Ultrafast generation and control of an electron vortex beam via chiral plasmonic near fields, Nat. Mater. **18**, 573 (2019).

[25] W. Cai, O. Reinhardt, I. Kaminer, and F. J. G. de Abajo, Efficient orbital angular momentum transfer between plasmons and free electrons, Phys. Rev. B **98**, 045424 (2018).

[26] I. Madan, V. Leccese, A. Mazur, F. Barantani, T. LaGrange, A. Sapozhnik, P. M. Tengdin, S. Gargiulo, E. Rotunno, J.-C. Olaya, I. Kaminer, V. Grillo, F. J. G. de Abajo, F. Carbone, and G. M. Vanacore, Ultrafast transverse modulation of free electrons by interaction with shaped optical fields, ACS Photonics **9**, 3215 (2022).

[27] F. J. García de Abajo, B. Barwick, and F. Carbone, Electron diffraction by plasmon waves, Phys. Rev. B **94**, 041404 (2016).

[28] S. Tsesses, R. Dahan, K. Wang, T. Bucher, K. Cohen, O. Reinhardt, G. Bartal, and I. Kaminer, Tunable photon-induced spatial modulation of free electrons, Nat. Mater. **22**, 345 (2023).

[29] A. Feist, K. E. Echternkamp, J. Schauss, S. V. Yalunin, S. Schäfer, and C. Ropers, Quantum coherent optical phase modulation in an ultrafast transmission electron microscope, Nature (London) **521**, 200 (2015).

[30] R. Dahan, S. Nehemia, M. Shentcis, O. Reinhardt, Y. Adiv, X. Shi, O. Be'er, M. H. Lynch, Y. Kurman, K. Wang, and I. Kaminer, Resonant phase-matching between a light wave and a free-electron wavefunction, Nat. Phys. **16**, 1123 (2020).

[31] T. Plettner, R. L. Byer, E. Colby, B. Cowan, C. M. S. Sears, J. E. Spencer, and R. H. Siemann, Visible-laser acceleration of relativistic electrons in a semi-infinite vacuum, Phys. Rev. Lett. **95**, 134801 (2005).

[32] F. O. Kirchner, A. Gliserin, F. Krausz, and P. Baum, Laser streaking of free electrons at 25 keV, Nat. Photon. **8**, 52 (2014).

[33] Y. Morimoto and P. Baum, Attosecond control of electron beams at dielectric and absorbing membranes, Phys. Rev. A **97**, 033815 (2018).

[34] Y. Adiv, K. Wang, R. Dahan, P. Broaddus, Y. Miao, D. Black, K. Leedle, R. L. Byer, O. Solgaard, R. J. England, and I. Kaminer, Quantum nature of dielectric laser accelerators, Phys. Rev. X **11**, 041042 (2021).

[35] C. Zhu, D. Zheng, H. Wang, M. Zhang, Z. Li, S. Sun, P. Xu, H. Tian, Z. Li, H. Yang, and J. Li, Development of analytical ultrafast transmission electron microscopy based on laser-driven Schottky field emission, Ultramicroscopy **209**, 112887 (2020).

[36] R. H. Pantell and M. A. Piestrup, Free-electron momentum modulation by means of limited interaction length with light, Appl. Phys. Lett. **32**, 781 (1978).

[37] T. Mackay and A. Lakhtakia, *The Transfer-Matrix Method in Electromagnetics and Optics* (Springer, Cham, 2020), Chap. 3, p. 51.

[38] Y. Jiang, S. Pillai, and M. A. Green, Realistic silver optical constants for plasmonics, Sci. Rep. **6**, 30605 (2016).

[39] H. R. Philipp, Optical properties of silicon nitride, J. Electrochem. Soc. **120**, 295 (1973).